Multimode Digital Control of a Suspended Polysilicon Microstructure

Gary K. Fedder, *Member, IEEE,* and Roger T. Howe, *Fellow, IEEE*

Abstract—**Digital control of a suspended 360 μm × 380 μm × 1.6 μm-thick surface-micromachined polysilicon plate is demonstrated in three degrees of freedom, with application to multimode accelerometers, vibratory rate gyroscopes, and actively positioned micromirrors. Plate displacement about the 2.2 μm nominal position above the substrate is measured with shielded capacitive sensors connected to CMOS buffer circuits fabricated adjacent to the microstructure. Four micromechanical sigma-delta loops are used to control eight electrostatic actuators that drive the plate vertically (z) and in out-of-plane rotation (θ and ϕ). Resonant frequencies are 2.7 kHz for the θ rotational mode and 3.7 kHz for both z and ϕ modes. The system is evaluated using a mixed mechanical/electromechanical/circuit simulation in SPICE. Closed-loop transient simulation of a 150-Hz square-wave position input signal is in good agreement with experimental results. Squeeze-film damping limits the plate slew rate to 0.83 mm/s in air. Position is controlled to within ±25 nm, being limited by quantization noise at the 50 kHz sampling rate. [192]**

I. Introduction

DIGITAL CONTROL of polysilicon surface-micromachined structures involves the use of electrostatic force-feedback generated from discrete voltage levels. Prior work has focused exclusively on sigma-delta (Σ-Δ) force-balanced control of single-mode microaccelerometers [1]–[5]. MEMS applications such as vibratory rate gyroscopes, multiaxis accelerometers, and actively positioned mirrors require control of multiple degrees of freedom. In this paper, we present an integrated testbed for research in digital control of a suspended polysilicon plate having three degrees of freedom.

Design of multimode closed-loop MEMS requires simulation of mixed analog–digital systems with nonlinear electromechanical elements. We have developed coupled mechanical/electromechanical/circuit time-domain simulations to evaluate design tradeoffs in the testbed. The behavioral simulations are implemented in SPICE so that microelectromechanical models and transistor-level circuit models can be easily integrated together in one simulation. Models of rigid-body mechanical modes, position sensors, and electrostatic actuators are implemented as subcircuits. By maintaining a modular description of each micromechanical element, models can be improved at a later time without changing the system-level definition. The behavioral simulation methods can be used in the design of specific inertial-sensing and micropositioning applications. Experimental verification of models and simulations for multimode Σ-Δ control is achieved by comparing the closed-loop step response of the testbed in air with the simulation results. Underdamped system dynamics of the testbed at low pressures are reported in [6].

The micromechanical Σ-Δ control architecture, shown in Fig. 1, is based on the high-frequency one-bit comparison between the output of a position sensor and an external reference, which generates a serial bitstream at the sampling frequency, f_s [7]. Digital signal processing followed by digital-to-analog conversion results in a stream of high-frequency voltage pulses, which are applied to an electrostatic actuator to generate the feedback force, F_{fb}. Frequency components of the feedback above mechanical resonance are attenuated by the micromechanical mass-spring damper. With proper attention to stability of the digital control loop, the position is stabilized, on average, at the position corresponding to the reference input. Sigma-Delta control strategies linearize the voltage dependence of the electrostatic force by only applying two quantized voltage levels to the actuators [1]. In addition to inherent linearity, Σ-Δ control offers large dynamic range and eliminates the need for precision position sensing. Digital control of a surface-micromachined structure, however, requires integration of at least the capacitive position-sense amplifiers in order to eliminate most of the signal attenuation due to parasitic capacitance [2]. The critical circuit design issues are the position-sensor sensitivity and speed to reduce the quantization noise.

II. Testbed Description

A. System Overview

A rendering of one quarter of the testbed is shown in Fig. 2. A polysilicon plate, which measures 360 μm × 380 μm × 1.6 μm in thickness, is suspended 2.2 μm above the substrate by four serpentine springs. The springs passively constrain lateral motion of the plate. Spring compliances can be configured in seven different ways by selectively cutting polysilicon fuses [8], which anchor the springs in several locations. The testbed plate is perforated with 580 4 μm by 4 μm holes spaced 16 μm apart. Four additional 64 μm by 24 μm slots allow room for

Manuscript received December 28, 1995; revised May 28, 1996. Subject Editor, E. Obermeier. This work was supported by the Berkeley Sensor & Actuator Center, an NSF/Industry/University Cooperative Research Center, and by the DARPA MEMS program.

G. K. Fedder was with the Berkeley Sensor & Actuator Center, Department of Electrical Engineering and Computer Science, University of California, Berkeley, Berkeley, CA 94720-1770 USA. He is now with the Department of Electrical and Computer Engineering and the Robotics Institute, Carnegie Mellon University, Pittsburgh, PA 15213-3890 USA.

R. T. Howe is with the Berkeley Sensor & Actuator Center, Department of Electrical Engineering and Computer Science, University of California at Berkeley, Berkeley, CA 94720-1770 USA.

Publisher Item Identifier S 1057-7157(96)08840-3.

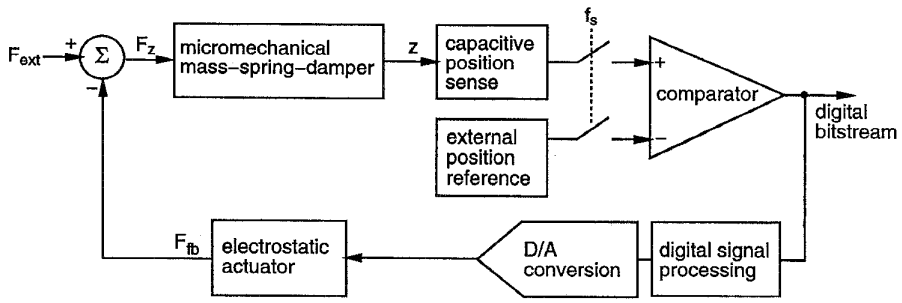

Fig. 1. Block diagram of the micromechanical Σ–Δ architecture.

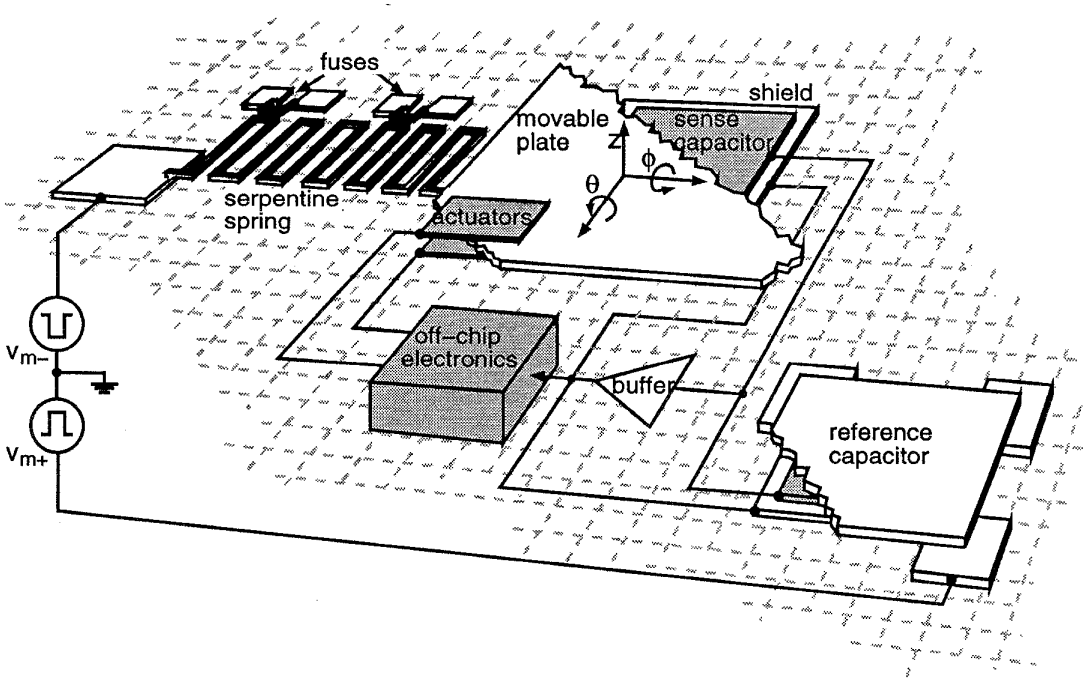

Fig. 2. Schematic drawing of one quarter of the integrated testbed.

external probing and manipulation. The plate is overdamped at room-ambient pressure; damping can be reduced to nearly zero by reducing the pressure. Residual damping in vacuum is the polysilicon structural damping, which is very small [9].

Vertical position, z, and angular rotation about the lateral axes, θ and ϕ, are controlled by four digital feedback loops. A parallel-plate vertical-position sense capacitor is located under each quadrant of the plate, forming a bridge with a fixed reference capacitor. Use of a driven shield electrode, together with an integrated CMOS buffer amplifier, are desirable for sensitive detection of the voltage change on the high-impedance node of the capacitive bridge. Off-chip Σ-Δ electronics supply digital feedback to electrostatic actuators at each corner of the plate.

Fig. 3 is an optical micrograph of the die, showing the micromechanical elements integrated with the CMOS circuitry. Reference capacitors are made from rigidly supported micromechanical structures that match the sense capacitor layout. Variable gain differential amplifiers, included in the layout, suffer from a design error and are not used in the system. The eight reference capacitors located at the upper and lower corners of the layout are associated with the differential amplifiers and are also not used. Bias circuitry is shared by the four buffer amplifiers. An expanded view of the polysilicon plate is shown in Fig. 4. Two comb drives, located on two opposing sides of the plate, provide both a vertical levitation force and a lateral force for displacements up to 10 μm. Each comb has 49 2-μm wide, 10μm long fingers. The four capacitive position sensors underneath the plate are identified, along with the upper and lower parallel-plate feedback actuators.

A block diagram of one of the four independent feedback channels is shown in Fig. 5. Each movable sense capacitor, C_s, forms a voltage divider with a corresponding fixed reference capacitor, C_r. Balanced square-wave voltage signals, v_{m+} and v_{m-}, provide ±300 mV modulation across the divider with

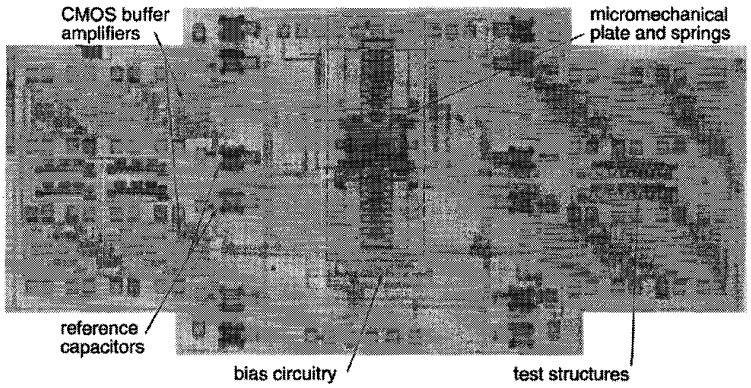

Fig. 3. Optical photograph of the integrated testbed. The dashed rectangle delimits the area shown in Fig. 4.

a maximum frequency of 100 kHz. A minimum area diode is connected to the buffer input and biases the dc voltage to ground. Diode biasing has been previously used in the capacitive sensing circuit for a micromachined vibrating ring gyroscope [10] and for a single-mode microaccelerometer [2]. The buffer output, v_s, is routed off-chip, demodulated, and amplified to generate a signal proportional to the peak-to-peak buffer output, v_{pp}. This signal is compared with an external position reference voltage, v_{ref}, quantizing the plate position into two states. The external reference enables multimode position control, self-test, and offset trim. The comparator output drives a level-shifting network, which generates feedback voltages containing a difference term to stabilize underdamped mechanical systems. Feedback voltage levels are adjustable, allowing experimentation with values of full-scale force and compensation. These signals are sent on-chip to the upper and lower parallel-plate actuators, C_u and C_l, respectively. Digital bitstreams from the comparators are filtered and combined to form multimode acceleration sense signals.

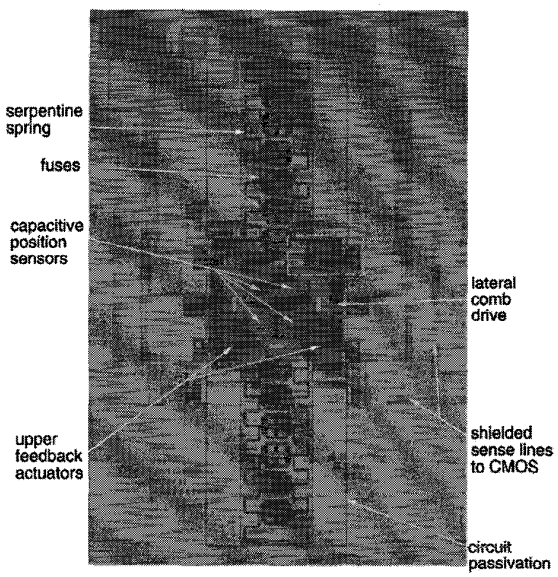

Fig. 4. Optical photograph showing an expanded view of the polysilicon plate and serpentine springs. The white dashed rectangle delimits the area shown in Fig. 7.

B. Fabrication Issues

Fabrication of the integrated testbed utilizes the Berkeley MICS process: a p-well 3 μm CMOS process integrated with polysilicon microstructures [11]. A MICS process cross section is shown in Fig. 6. Sputtered tungsten interconnect with TiN/$TiSi_2$ contacts is necessary to withstand the temperature of subsequent microstructure processing steps. We have extended the original MICS process to include a second structural polysilicon layer (sensor poly-3). The upper feedback actuator is made from the second structural layer and shown in Fig. 7. In order to avoid polysilicon stringer formation, the 2.7-μm thick sacrificial layer underlying the upper electrode is planarized by using a sandwich of spin-on glass (SOG) film and phosphosilicate glass (PSG), which is rapid-thermal annealed at 900°C [12]. Upper limit stops, which prevent shorting of the actuators, are also made from the second structural layer. The spacer PSG acts as passivation for the tungsten metallization and is only removed around the microstructure areas. Microstructure release in 5:1 BHF is done in darkness to avoid electrochemical etching of the polysilicon bonding pads.

III. Modeling and Simulation

A. Mechanical Modeling

The resonant modes of the testbed plate are determined from a linear finite-element analysis [13], using three-node quadratic beam elements for the springs and nine-node quadrilateral shell elements for the plate. Fig. 8 displays the lowest eight modes for the plate, where each spring is configured with one fuse cut. Resonant frequency values of the lowest four modes, θ-rotation (rotation about the x axis), z-translation, ϕ-rotation (rotation about the y axis), and x-translation are between 2.8 and 3.9 kHz. The other two rigid-body modes of the plate, y-translation and ψ-rotation (rotation about the z axis), have slightly larger values of resonant frequency. Plate bending modes and spring vibrational modes have resonant frequency values that are over 24 times higher than the fundamental mode.

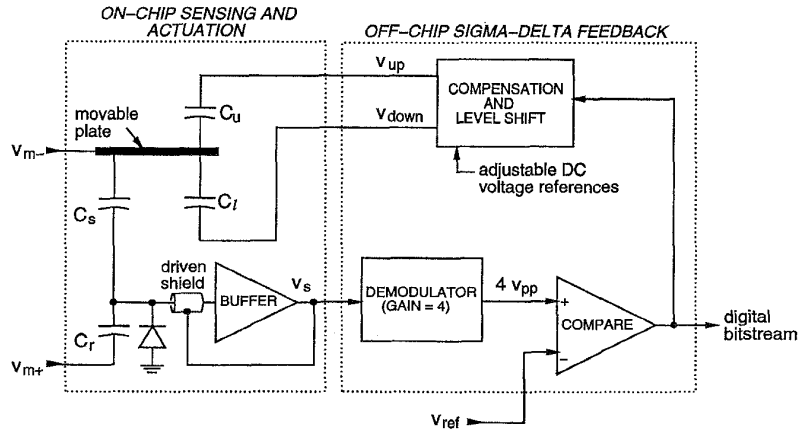

Fig. 5. Block diagram of one quarter of the integrated testbed.

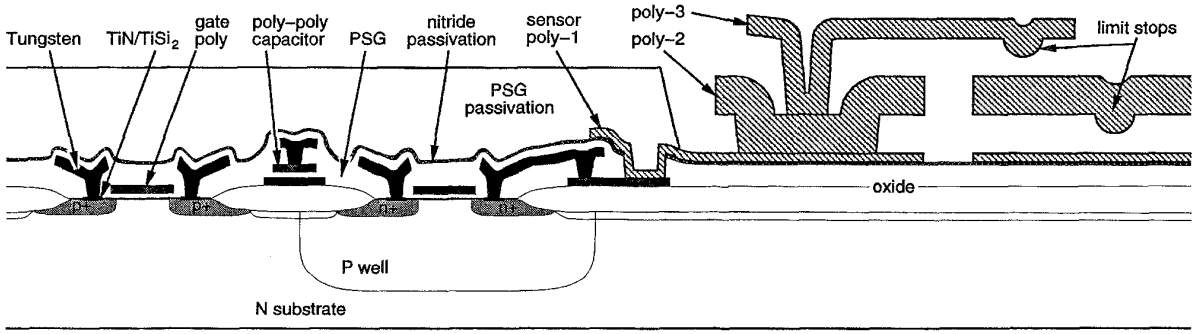

Fig. 6. MICS process cross-section.

There are three controllable mechanical modes of the plate: vertical displacement, Δz, (defined relative to the fabricated spacer gap, $z_o = 2.2\ \mu$m) and the two rotations, θ and ϕ, about the lateral axes. These modes are modeled with rigid-body, mass-spring-damper transfer functions

$$H_z(s) = F_z(s)/\Delta z(s) = m(s^2 + 2\zeta_z\omega_z s + \omega_z^2) \quad (1)$$

$$H_\theta(s) = T_\theta(s)/\theta(s) = I_\theta(s^2 + 2\zeta_\theta\omega_\theta s + \omega_\theta^2) \quad (2)$$

$$H_\phi(s) = T_\phi(s)/\phi(s) = I_\phi(s^2 + 2\zeta_\phi\omega_\phi s + \omega_\phi^2) \quad (3)$$

where F_z, T_θ, T_ϕ are external force and torques on the plate, m, I_θ, and I_ϕ are plate mass and mass moments of inertia, ζ_z, ζ_θ, and ζ_ϕ are dimensionless damping factors, and ω_z, ω_θ, and ω_ϕ are resonant frequencies of each mode. For an underdamped system ($\zeta \ll 1/\sqrt{2}$), the quality factor is given by $Q = 1/(2\zeta)$. The testbed system is analyzed by transforming the four quad-symmetric feedback loops into the three modes. Since there are four feedback loops and only three controllable modes, however, the system is over-constrained. Offsets must be precisely adjusted to avoid undesired oscillations or force limiting in one of the loops. Alternatively, one of the loops can be disabled to avoid the over-constraint problem.

Each mechanical mode is represented by an equivalent series LCR circuit, as shown in Fig. 9 for the vertical mode. The damping coefficient is $B_z = 2m\zeta_z\omega_z$, and the spring constant is $k_z = m\omega_z^2$. The capacitor charge in the equivalent circuit is proportional to the modal displacement. A scaling factor, A, is needed to keep the electrical impedance values of the LCR circuit from being very small, thereby avoiding numerical convergence problems in the simulations. For surface-micromachined devices, a suitable value for A is 10^6.

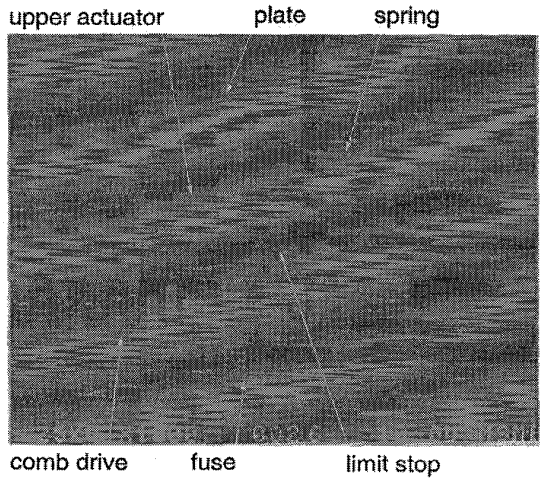

Fig. 7. SEM of one corner of the movable plate, suspended below the upper actuator cantilever.

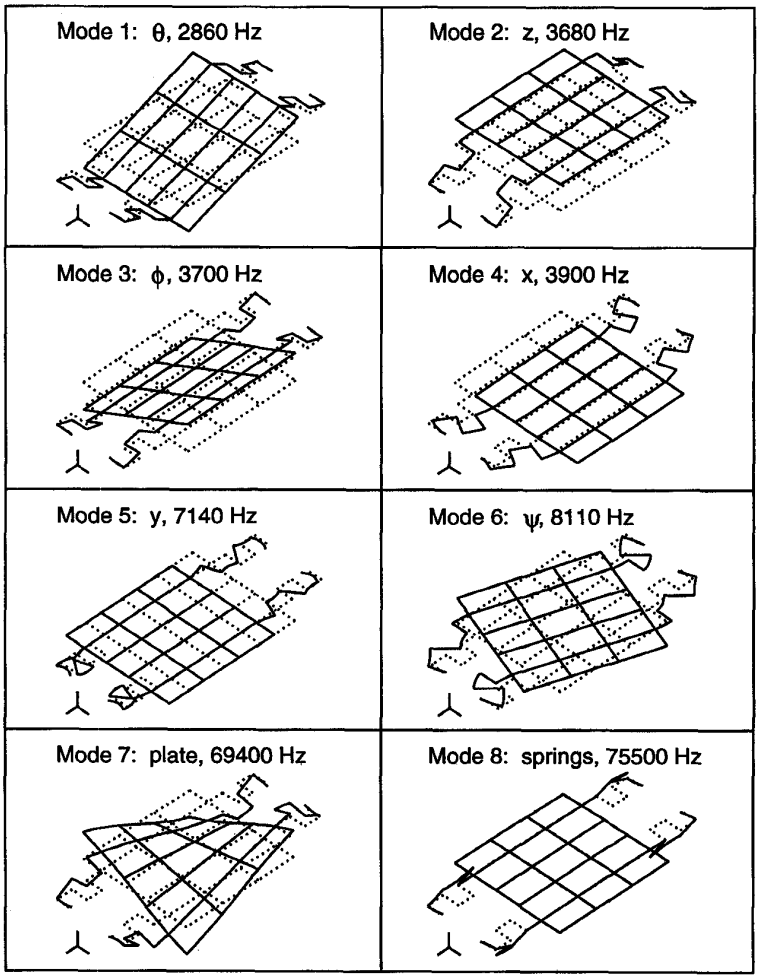

Fig. 8. Illustration of the eight lowest mechanical modes of the testbed, where each spring is configured with one fuse cut.

TABLE I
MECHANICAL PARAMETER VALUES AND THE EQUIVALENT SPICE PARAMETER VALUES FOR THE TESTBED UNDER TYPICAL OPERATING CONDITIONS, WHERE $A = 10^6$

Mechanical parameters:		Electrical parameters:
$m = 4.7 \times 10^{-10}$ kg		$L[m] = 0.47$ mH
$k_z = 0.25$ N/m		$C[k_z] = 4.0\ \mu$F
$B_z = 2.6 \times 10^{-4}$ N-s/m	$\Longleftrightarrow$	$R[B_z] = 260\ \Omega$
$F_z = 100$ nN		$V[F_z] = 0.1$ V
$z = 0.5\ \mu$m		$V[\Delta z] = 0.5$ V

Testbed parameter values for typical operating conditions are given in Table I.

B. Parallel-Plate Capacitors

The electrostatic microactuators and capacitive position sensors are modeled as parallel-plate air-gap capacitors. For small angular displacements, the capacitance equation for the sensors and lower actuators is given by

$$C = \frac{\alpha_c \epsilon_o A_c}{z_{co} + \Delta z - x_{co}\phi + y_{co}\theta} \tag{4}$$

where $\epsilon_o = 8.854$ pF/m, A_c is the capacitor plate area, $[x_{co}, y_{co}, z_{co}]$ is the position of the center of the stator plate relative to the undisplaced center of the movable plate, and α_c is a form factor that accounts for fringing capacitance. A similar equation can be found for the upper actuators. The electrostatic force of the actuator plates and capacitive sensors acting in the vertical direction is

$$F_z = \begin{cases} \dfrac{-\alpha_f \epsilon_o A_c v_c^2}{2(z_{co} + \Delta z - x_{co}\phi + y_{co}\theta)^2}; & \text{for lower actuators} \\ \dfrac{+\alpha_f \epsilon_o A_c v_c^2}{2(z_{co} - \Delta z + x_{co}\phi - y_{co}\theta)^2}; & \text{for upper actuators} \end{cases} \tag{5}$$

where α_f is the fringing-field force factor and v_c is the capacitor voltage. Electrostatic torque acting on the plate is calculated by multiplying the force by the lateral distance of the capacitor plate from the center of the suspended

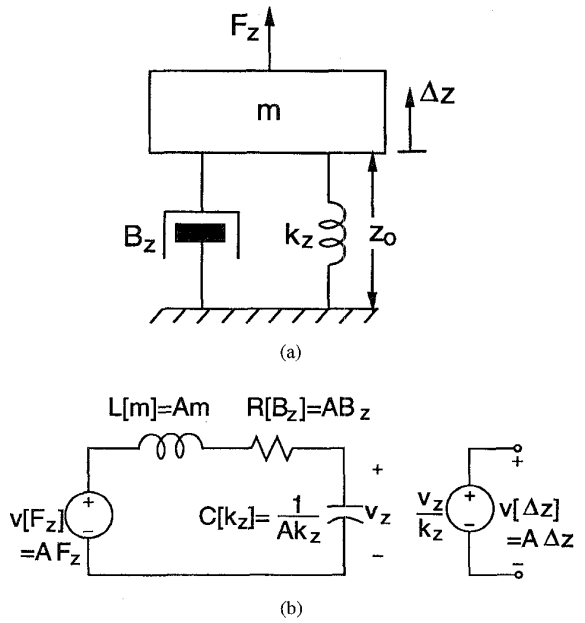

Fig. 9. Electrical analogy to a second-order mechanical system. (a) Mechanical mass-spring-damper (Δz mode). (b) Equivalent LCR circuit where impedance values are scaled by the factor A.

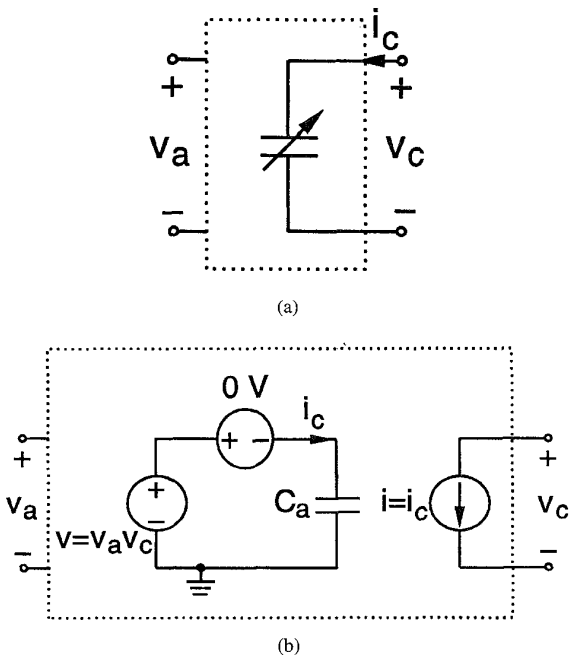

Fig. 10. Time-varying capacitor (TVC) model in SPICE. (a) Circuit instance. (b) Subcircuit model.

plate. Fringing capacitance from holes in the plates and from the plate edges varies with vertical position, and, therefore, affects the electrostatic force and torque. Appropriate values for the fringing-field form factors are determined from two-dimensional electrostatic finite-element analysis.

The micromechanical capacitors are modeled in SPICE with the time-varying-capacitor (TVC) subcircuit shown in Fig. 10. The TVC I–V characteristic is given by

$$i_c = \frac{d}{dt}(C_a v_a v_c) \tag{6}$$

where C_a is a capacitance scaling factor and v_a is a voltage that specifies the instantaneous scaled capacitance value. The quantity $C_a v_a$ in (6) represents the time-varying capacitance in units of farads. A nonlinear voltage source converts the product $v_a v_c$ to a voltage that drives the capacitor C_a. The current through C_a is measured with a zero-volt voltage source and mirrored back through the capacitor port using a dependent current source. Since surface-micromechanical capacitor values are usually between 1 fF and 1 pF, the capacitance scaling factor is set to 1 pF in the testbed simulations. The TVC model and the electrostatic force relation (5) are combined to form an electromechanical parallel-plate-capacitor subcircuit. This subcircuit can be implemented in any version of SPICE that supports nonlinear voltage-controlled voltage sources.

C. Position Sense Circuit

A cross section of a parallel-plate sense capacitor is shown in Fig. 11(a). The sense capacitance, C_s, has a variable parallel-plate component, C_{sv}, and a fixed component, C_{sf}, due to interconnect overlap with the modulation source interconnect. Most of the interconnect on the high-impedance node is surrounded by a driven shield having capacitance C_{shld}. The capacitance between the upper plate and substrate, C_m, and the capacitance between the shield and substrate, C_{sub}, are driven by low-impedance sources and do not affect the sensor signal. An equivalent circuit model of one position sensor is shown in Fig. 11(b). Assuming a balanced square-wave modulation source with amplitude V_m, the sensor peak-to-peak output is

$$v_{pp} = 2G_o V_m \left(\frac{C_r - C_s}{C_r + C_s + C_p} \right) \tag{7}$$

where G_o is the buffer gain and C_p is the effective parasitic capacitance loading the high-impedance node.

The buffer circuit is a very simple solution for capacitive position sensing and is capable of detecting Brownian noise of the testbed. A switched-capacitor circuit is an alternative means of capacitive detection, but requires careful design to reduce noise from charge-injection onto the small micromechanical sense capacitors [4]. The CMOS unity-gain buffer circuit shown in Fig. 12 is an improved version of a previous design [2]. The single-stage amplifier has a moderate open-loop voltage gain, but the circuit is stable even when driving large capacitive loads. A 20-kΩ external resistor supplies bias current for the circuit. Load current in each branch is matched with the p-channel current mirror (M5–M6). The differential stage drives a substantial on-chip load capacitance, C_{sub}, due to the interconnect and shield, and a source follower (M9–M10) drives the off-chip capacitance.

A key design issue is minimization of buffer input capacitance, which adds directly to parasitic capacitance and decreases the output sensitivity. The requirement of a reasonable open-loop gain value dictates that the input transistor gate

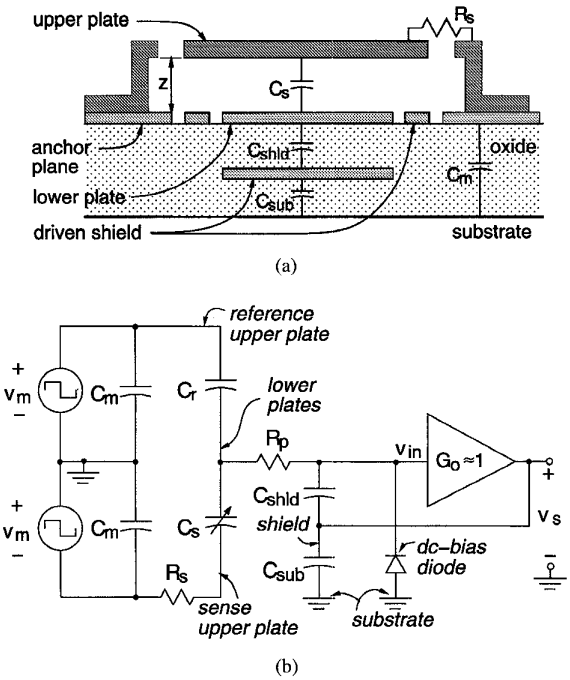

Fig. 11. Capacitive position sensor. (a) Schematic cross section of one micromechanical parallel-plate sense capacitor, C_s. Parasitic capacitance to ground is reduced by surrounding the bottom sense plate with a driven shield and guard ring. The upper plate is connected to the anchor plane through the spring suspension, which has resistance R_s. (b) Equivalent circuit model. A capacitive voltage divider is formed by connecting the sense capacitor to a matched reference capacitor, C_r, which is not shown in (a). Interconnect to the buffer amplifier has resistance, R_p.

area cannot be made arbitrarily small. Buffer input capacitance is reduced by forcing the source, drain, and body voltages of M1 to track the input gate voltage. Since a p-well CMOS process is used, we can connect the input-transistor well and source together, thereby reducing the effect of body voltage on input capacitance. Transistors M3 and M4 are included to mirror the output voltage to the drain of M1.

The dc buffer gain, input capacitance, and bandwidth are found from a low-frequency, small-signal equivalent analysis of the circuit in Fig. 12

$$G_o \simeq \left(1+\frac{1}{g_{m1}r_{o6}}+\frac{1}{g_{m1}Z_L}\right)^{-1} \tag{8}$$

$$C_i \simeq \frac{C_{gs1}}{2g_{m1}}\left(\frac{1}{r_{o7}}+\frac{1}{r_{o6}}+\frac{1}{Z_L}\right) \tag{9}$$

$$f_o \simeq \frac{g_{m1}}{2\pi C_L} \tag{10}$$

where g_{mi} and r_{oi} are the transconductance and the output resistance of the ith transistor, respectively, C_{gs1} is the gate-to-source capacitance of M1, Z_L is the output load impedance, and C_L is the load capacitance. Table II lists the buffer gain, capacitance, and bandwidth values determined using the analytical equations alongside values determined using the HSPICE [14] simulation program. The load capacitance is assumed to be 3 pF in the bandwidth calculation. The analytic and simulated results are in good agreement.

TABLE II
PERFORMANCE SPECIFICATIONS FOR THE UNITY-GAIN BUFFER CALCULATED FROM ANALYTIC ANALYSIS AND HSPICE [14] SIMULATION

Unity-Gain Buffer Circuit			
specification	symbol	analytic	HSPICE
dc gain	G_o	0.9976	0.9965
input capacitance	C_i	3.97 fF	4.32 fF
bandwidth	f_o	20.4 MHz	20.2 MHz

The effective parasitic capacitance

$$C_p = (1-G_o)C_{\text{shld}} + C_i + C_d \tag{11}$$

has three components: the effective shield capacitance, the buffer input capacitance (C_i), and the input diode junction capacitance (C_d). The input diode has an n^+ diffusion area of 135 μm^2, corresponding to a junction capacitance of 71 fF at zero bias. For the testbed position sensors, the shield capacitance is approximately 1 pF. Using the gain value in Table II, the effective shield capacitance is reduced to 2.4 fF. Therefore, the diode capacitance term in (11) is much larger than the contributions from both the driven-shield and the buffer and is responsible for a decrease in sensitivity of the position sense circuit.

D. Testbed Simulation Block Diagram

A block diagram of the testbed SPICE simulation is given in Fig. 13. Force and torque applied to the plate are calculated by summing the voltage sources that represent the individual force and torque contributions from the actuator and sensor plates. The resulting voltage sums are connected to the equivalent LCR-circuit model for each respective mode. Plate displacement and rotation are output as voltages $(v[\Delta z], v[\theta], v[\phi])$ from the LCR circuits and supplied as inputs to the parallel-plate capacitor subcircuit instances. The instantaneous sensor capacitance value in each of the four quadrants is found from (4) and is represented in the TVC subcircuit by the nonlinear voltage source, $v_a[C_{si}]; i = 1,2,3,4$. For example

$$v_a[C_{s1}] = \frac{\alpha_s \epsilon_o A_s}{z_{so} + v[\Delta z] - x_{so}v[\phi] + y_{so}v[\theta]} \tag{12}$$

where $\alpha_s = 1, A_s = 10^4\ \mu m^2, x_{so} = y_{so} = 60\ \mu m$, and $z_{so} = 2.2\ \mu m$. The upper and lower actuator capacitors are expressed by similar equations. Both the capacitive divider and the unity-gain buffer circuit for each quadrant are modeled at the transistor level. The demodulator and comparator are represented by simple behavioral models.

Averaged feedback force signals can be generated by passing each of the four Σ-Δ bitstreams, represented in analog form by v_{up1} to v_{up4} in Fig. 13, through independent digital low-pass filters. Assuming small displacements, the generalized force for each mode (F_z, τ_θ, and τ_ϕ) can then be extracted by summing or differencing the signals appropriately. For example, F_z is proportional to the sum of all four averaged bitstreams.

An important drawback of SPICE is the long time to necessary complete a transient simulation. An 8-ms simulation of the testbed, corresponding to 400 cycles at a 50-kHz

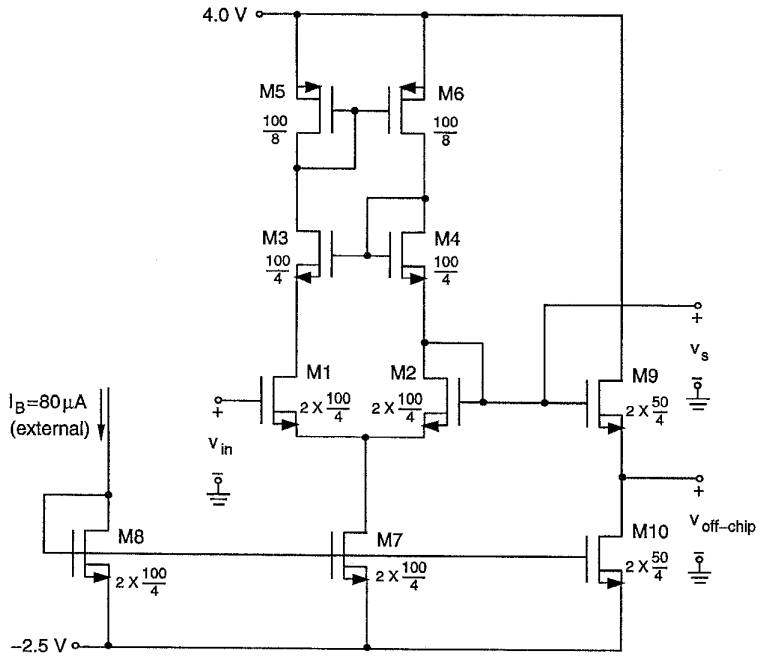

Fig. 12. Unity gain buffer circuit schematic.

sampling rate, takes about 44 min of CPU time on an IBM RS/6000 580H with 512 Mbytes of RAM. If detailed circuit simulation is not required, then system simulation using a behavioral model for the position-sensor is a speedy alternative [6].

IV. Noise Analysis

A. Overview

Noise in the testbed system can be separated into two categories: electronic noise voltage that corrupts the position sensor signal and mechanical noise force that acts on the plate. Individual noise contributions come from mechanical thermal noise, electrostatic actuator noise, circuit noise, and Σ–Δ quantization noise. Interpretation of the noise analysis depends on the application. All noise contributions from dc up to the modulation frequency must be included in a general analysis.

In microaccelerometer applications, low-frequency equivalent input noise force sets the sensitivity limit for the sensor. The signal band of interest in accelerometry is approximately dc to 1 kHz, so the high-frequency equivalent noise force can be electronically filtered from the output signal. In the testbed capacitive sensing scheme, the position signal is amplitude modulated at a high carrier frequency. Any low-frequency components of the position-sensor noise are filtered during the subsequent demodulation. Therefore, only components of the position-sensor noise voltage around the carrier frequency affect the accelerometer sensitivity.

In micropositioner applications, total input noise position limits the positioning stability. Low-frequency noise force contributions do not affect performance, since the position at low frequencies is nulled in closed-loop operation. High-frequency force-feedback pulses generated by the Σ–Δ loops are the primary source of chatter, which limits the positioning stability of the plate.

B. Position-Sensor Noise Voltage

Noise voltage associated with the capacitive position sensor is generated by the buffer circuit, the dc bias diode, and interconnect resistance. Buffer noise is contributed from transistors M1, M2, M5, and M6 in Fig. 12. The bias-current transistors (M7 and M8) only affect the common-mode current, and transistors M3 and M4 are cascoded, so none of these devices add to the output noise. Additional noise from the source-follower stage (transistors M8, M9, and M10) will not be included in the analysis. The equivalent input-referred noise voltage, $\overline{v_{\mathrm{eq},u}^2}$, for the unity-gain buffer without the driven shield is

$$\frac{\overline{v_{\mathrm{eq},u}^2}}{\Delta f} = \frac{16k_BT}{3g_{m1}}\left(1+\sqrt{\frac{k_p'(W/L)_{\mathrm{M6}}}{k_n'(W/L)_{\mathrm{M1}}}}\right) + \frac{2K_p}{C_{\mathrm{ox}}(WL)_{\mathrm{M1}}f}\left(1+\frac{K_pk_p'L_{\mathrm{M1}}^2}{K_nk_n'L_{\mathrm{M6}}^2}\right) \quad (13)$$

where k_B is Boltzmann's constant (1.381×10^{-23} J/K), T is absolute temperature, W refers to the channel width, L refers to the channel length, C_{ox} is the gate oxide capacitance per unit area, k_n' and k_p' are the intrinsic transconductance factors, and K_n and K_p are the flicker coefficients for the n-channel and p-channel transistors, respectively. The symbol $\overline{v_{\mathrm{eq}}^2}$ denotes the mean-square of the noise spectral distribution where Δf is a small bandwidth.

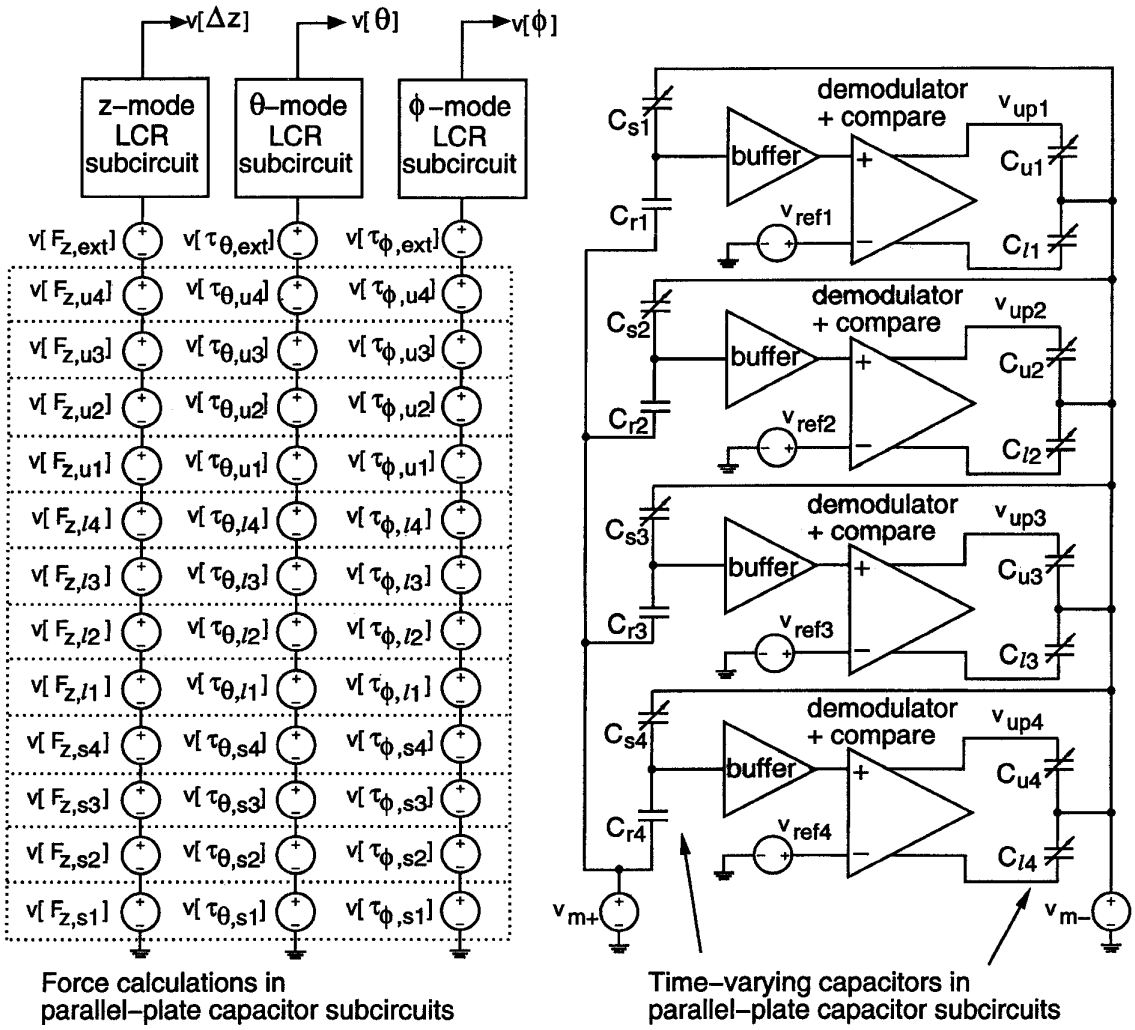

Fig. 13. Block diagram of the testbed SPICE deck. The four quadrants of the plate are denoted by the subscripts 1, 2, 3, and 4.

The buffer equivalent noise voltage, $\overline{v_{\mathrm{eq},u}^2}$, is in series with the feedback connection through the shield capacitor. Assuming an ideal unity gain, the equivalent input-referred noise voltage for the buffer circuit with the driven shield is

$$\overline{v_{\mathrm{eq},b}^2} = \left(\frac{C_{\mathrm{shld}} + C_r + C_s + C_i + C_d}{C_r + C_s + C_i + C_d}\right)^2 \overline{v_{\mathrm{eq},u}^2}. \tag{14}$$

The noise is amplified by the capacitive feedback. For the testbed circuit, the driven-shield configuration amplifies the noise to a level about six times the noise value of the buffer without a driven shield.

Noise current in the dc bias diode has both shot noise and flicker noise components

$$\frac{\overline{i_d^2}}{\Delta f} = 2qI_D + K_d\frac{I_D}{f} \tag{15}$$

where $q = 1.602 \times 10^{-19}$C, K_d is the flicker noise coefficient, and I_D is the direct carrier current in the diode. In darkness, a direct diode current results from photocurrent generated by background radiation and from dark current due to thermal generation of electron-hole pairs in the depletion region. Additional photocurrent is generated during testbed operation under an optical microscope. Since the diode is connected in an open-circuit configuration, the direct carrier current is twice the short-circuit current. An ac diode current exists due to the modulation signal impressed across the junction capacitance. This current does not contribute to noise, however, since carriers do not flow directly across the junction. The noise current can be expressed as an equivalent noise voltage

$$\frac{\overline{v_{\mathrm{eq},d}^2}}{\Delta f} = \frac{I_D}{[2\pi f(C_r + C_s + C_p)]^2 + 1/R_j^2}\left(2q + \frac{K_d}{f}\right) \tag{16}$$

where R_j is the diode small-signal junction resistance. Effective surface conduction between the high-impedance node and the surrounding shield is considered negligible, but can be included in the analysis by introducing a resistance in parallel with R_j.

Interconnect from the micromechanical sense capacitors is formed from resistive polysilicon layers, which generate a thermal noise voltage. Electrical connection to the movable

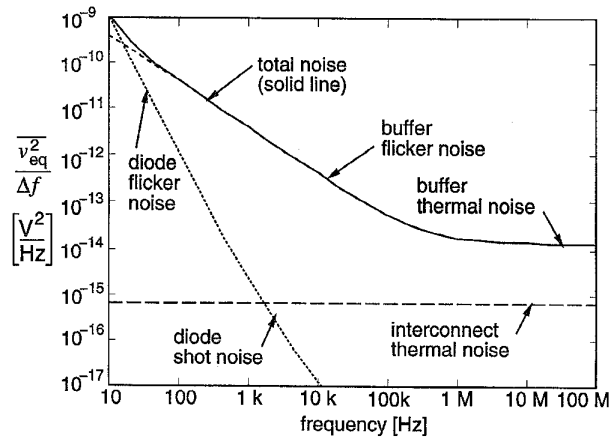

Fig. 14. Equivalent noise voltage spectral density of the position-sensor circuit.

upper plate must be made through slender beams of the polysilicon suspension. The suspension has a series resistance, R_s, whose value ranges from 1 kΩ to 100 kΩ, depending on the chosen spring configuration. An interconnect resistance R_p of approximately 10 kΩ exists between the high-impedance node of the divider and the buffer input. All other interconnect resistances are negligible. The equivalent noise voltage from parasitic resistance, referred to the buffer input, is

$$\frac{\overline{v_R^2}}{\Delta f} = 4k_BT\left\{\left(\frac{C_s}{C_r + C_s + C_p}\right)^2 R_s + R_p\right\}. \tag{17}$$

The total position-sensor noise voltage is found by summing (14), (16), and (17). A representative plot of the equivalent noise voltage spectral density referred to the buffer input is shown in Fig. 14 for $K_n = K_p = 3 \times 10^{-24}$ V^2 – F, $K_d = 3 \times 10^{-16}$ A, $R_s = R_p = 10$ kΩ, $C_s = C_r = 45$ fF, $R_j = 10^{12}$ Ω, and $I_D = 10^{-15}$ A. Thermal noise from the buffer transistors dominates at frequencies above 500 kHz, equivalent diode flicker noise voltage dominates at frequencies below 15 Hz, and equivalent transistor flicker noise dominates at intermediate frequencies. The interconnect noise is negligible. Low-frequency components of position-sensor noise voltage are filtered out of the output signal using correlated double sampling in the demodulator circuit. The equivalent $1/f$ noise sets a lower bound on the carrier frequency value of approximately 500 kHz for high-frequency thermal noise voltage to dominate. Equivalent diode noise voltage is calculated using a conservative estimate of the direct diode current in darkness. The diode noise contribution increases linearly with the additional photocurrent due to operation under an optical microscope. A direct comparison of noise voltage measurements in darkness and in light was not performed, however.

C. Brownian Noise Force

Air molecules impinging on the micromechanical plate give rise to thermal (Brownian) noise forces and torques proportional to damping. In thermal equilibrium, each energy storage mode of the plate must have an average thermal fluctuation energy of $\frac{1}{2}k_BT$ [15]. For the Δz mode, the Brownian noise force is proportional to the damping coefficient

$$\frac{\overline{f_{B_z}^2}}{\Delta f} = 4k_BTB_z = 4k_BT(2m\zeta_z\omega_z). \tag{18}$$

Similar equations describe the Brownian noise torques about the x-axis and y-axis.

For accelerometer applications, Brownian noise is referred to an equivalent acceleration input

$$\frac{\overline{a_{\text{eq},B_z}^2}}{\Delta f} = 4k_BT\left(\frac{2\zeta_z\omega_z}{m}\right). \tag{19}$$

A larger proof mass gives a larger Brownian noise force, but also increases the external force signal. The net result is a decrease in equivalent noise acceleration. A large micromechanical plate is usually overdamped in air. Decreasing the squeeze-film damping by reducing the ambient pressure will lower the mechanical noise floor. Polysilicon micromechanical quality factors up to 80 000 have been reported [16], [17], which translates into greater than a 300-fold decrease in Brownian noise.

D. Electrostatic Actuator Noise Force

Another source of noise force acting on the plate arises from noise voltages that are impressed across the electrostatic actuators. An electrostatic actuator noise force is present on feedback actuators, sensor capacitors, and open-loop actuators such as the comb drives. Electrostatic force generated by these elements is equal to γV_a^2 where V_a is the applied dc voltage and γ is a proportionality constant with units of N/V^2. Noise force from unused electrostatic actuators is very small and can be neglected. For the upper and lower feedback actuators, the equivalent noise force is

$$\overline{f_{\text{eq},a}^2} = (2\gamma V_a)^2\overline{v_a^2} \tag{20}$$

where the actuator noise voltage, $\overline{v_a^2}$, is generated by interconnect resistance and is assumed to be much smaller than the applied voltage.

The total actuator noise cannot be found directly from (20) because the applied voltages on the feedback actuators are not pure dc signals and because noise is correlated between the upper and lower actuators. An estimate of noise force is found by using only terms arising from the dc components of the applied voltage and then subtracting the lower actuator noise from the upper actuator noise. A more precise noise analysis would account for the spectral content of the actuator feedback signals.

Actuator noise force from the capacitive sensors is generated by interconnect noise resistance and equivalent diode noise voltage. Equivalent circuit noise from the buffer transistors does not affect the voltage across the sensor capacitor and, therefore, does not contribute to the actuator noise force. The equivalent diode noise voltage plotted in Fig. 14 is much larger than the interconnect noise at frequencies below 2 kHz. The noise force contribution from the sensor capacitors is modulated at the sampling frequency, however, and the low-frequency diode noise force is shifted out of the acceleration

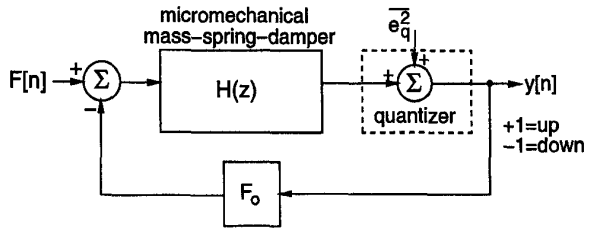

Fig. 15. Sampled-data representation of the Δz mode of the testbed. The one-bit quantizer is modeled as a source of white noise.

signal band. A substantial low-frequency equivalent noise force would have been present if the movable plate had been the high-impedance node, since then the diode noise would have been impressed directly across the feedback actuators.

E. Quantization Noise Force

Quantization noise is analyzed using the sampled-data representation of the Δz mode shown in Fig. 15. The micromechanical mass-spring-damper and the sampling switch are approximated by a second-order z-transform, $H(z)$

$$H(z) = \frac{K_n z^{-1}}{1 - \alpha z^{-1} + \beta z^{-2}} \tag{21}$$

where K_n is the loop gain normalization factor. The coefficients α and β are found directly from the impulse response of the mechanical system

$$\alpha = e^{-\zeta_z \omega_z T_s}\left(e^{\omega_z T_s\sqrt{\zeta_z^2-1}} + e^{-\omega_z T_s\sqrt{\zeta_z^2-1}}\right) \tag{22}$$

$$\beta = e^{-2\zeta_z \omega_z T_s} \tag{23}$$

where T_s is the sampling period. The high-gain nonlinear quantizer enforces a loop gain value of -1 at the Nyquist rate, $f_s/2$. This loop-gain approximation is valid for overdamped systems and for underdamped systems that are compensated and sampled at a frequency much higher than the resonant frequency. The quantizer is modeled as a source of additive white noise with a total mean-square noise given by $\Delta^2/12$ where Δ is the difference in the two quantizer output levels [7]. These two levels translate into a force of magnitude F_o pulling up or down on the plate. Quantization noise is limited in bandwidth to the Nyquist rate so the noise power is

$$\frac{\overline{e_q^2}}{\Delta f} = \left(\frac{\Delta^2}{6 f_s}\right). \tag{24}$$

The white-noise assumption neglects tones that may be present in the loop, however the simplified analysis provides insight into how system parameters affect the equivalent quantization noise force. More detailed noise analysis requires extensive mixed-mode simulations.

A relatively low sampling rate or large damping produces a lossy single-pole mechanical response below the Nyquist frequency, where $\alpha \approx e^{-\omega_n T_s/(2\zeta)}$ and β can be neglected. For the overdamped case, the equivalent low-frequency quantization noise force for the Δz mode is

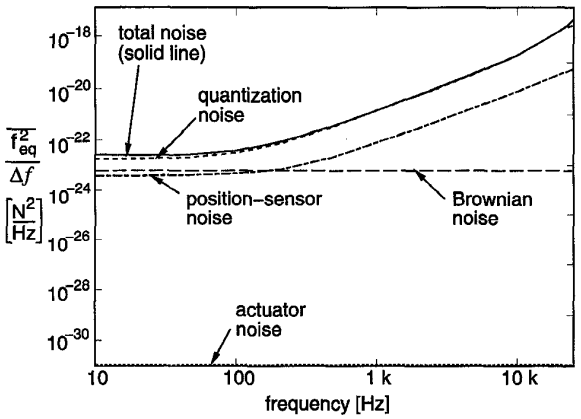

Fig. 16. Equivalent noise force spectral density of the testbed.

$$\frac{\overline{f_{\mathrm{eq},q}^2}}{\Delta f} \simeq F_o^2\left(\frac{\omega_z}{2\pi\zeta f_s}\right)^2 \frac{\overline{e_q^2}}{\Delta f} = F_o^2\left(\frac{\Delta^2}{12}\right)\frac{2 f_n^2}{\zeta^2 f_s^3} \tag{25}$$

where $\omega T_s \ll 1$ and $f_n = \omega_n/(2\pi)$. Doubling the sampling frequency results in a 9-dB noise reduction, as expected for a first-order Σ-Δ loop. Lowering the resonant frequency or increasing the damping will also reduce the low-frequency quantization noise force. The damping dependence on quantization noise is reversed from that of the Brownian noise, for $\zeta > 1$.

Equivalent low-frequency noise force for systems that are mechanically underdamped or have a high sampling rate is

$$\frac{\overline{f_{q,\mathrm{eq}}^2}}{\Delta f} \simeq F_o^2\left(\frac{\omega_n}{\pi f_s}\right)^4 \frac{\overline{e_q^2}}{\Delta f} = F_o^2\left(\frac{\Delta^2}{12}\right)\frac{f_n^4}{(f_s/2)^5}. \tag{26}$$

The low-frequency quantization noise force is reduced by 15 dB for each doubling of the sampling rate, which matches the performance of a conventional second-order Σ–Δ loop. There is a noise reduction of 12 dB/octave decrease in the resonant frequency, but the quantization noise force is insensitive to the mechanical quality factor.

F. Total System Noise

A representative plot of equivalent noise force spectral density is shown in Fig. 16 using the previous parameter values from Fig. 14. The low-frequency noise force is dominated by quantization noise, with the Brownian noise being about three times less significant. The total equivalent noise acceleration is 7.5 mg in a 50-Hz bandwidth (1 g = 9.8 m/s^2). Increasing the sampling rate decreases the quantization noise until eventually Brownian noise limits the minimum detectable acceleration to 3.6 mg in a 50-Hz bandwidth. Further improvements in acceleration sensitivity require reductions in equivalent noise voltage from the buffer transistors. The electrostatic actuator noise force is negligible in the testbed architecture.

For open-loop micropositioning applications, the Brownian noise force and actuator noise force generate an equivalent

noise position of the plate

$$\frac{\overline{z^2_{\mathrm{eq},B_z}}}{\Delta f} = 4k_BT\left(\frac{2\zeta_z}{m\omega_z^3}\right)\frac{1}{(1-\omega^2/\omega_z^2)+(2\zeta_z\omega/\omega_z)^2} \quad (27)$$

where the noise spectral density has the same frequency distribution as the mechanical mass-spring-damper. A resonance peak will occur in the equivalent noise position of underdamped systems. The total Brownian noise position for open-loop operation of the testbed in air is 0.56 nm.

In closed-loop testbed operation, the Brownian noise force and actuator noise force are detected and nulled at frequencies below the electrical bandwidth of the system. The total closed-loop equivalent noise position is calculated by referring the noise force spectral density in Fig. 16 to position and then integrating the noise up to the Nyquist rate, yielding a value of 9.8 nm. Quantization noise is the primary contributor to noise position during closed-loop operation. Increasing the sampling rate to 70 kHz will reduce the calculated quantization noise to below the Brownian noise limit. Improvements in the settling time of the external electronics are required, however, to operate at higher sampling frequencies. Alternatively, moving the feedback electronics on-chip would greatly reduce settling time and allow operation at very high sampling rates.

The total noise from the three excited modes will be split equally among each individual actuator noise force, due to the actuator symmetry. When force or torque for a given mode is extracted from the bitstreams, only the noise in that mode is present; the other modal noise contributions are canceled. For example, when all four actuator forces are summed, the correlated noise from the rotational modes is canceled. It is estimated that 2/3 (two of three modes) of the total quantization noise spectral density present on an individual actuator is correlated with respect to rotational modes in the other three actuators. The estimated correlated noise in an individual actuator bitstream is about 0.7 times the total noise of the vertical mode.

V. Experimental Results

One of the testbed devices was packaged in a 24-pin DIP and set into a custom fixture for testing at a probe station. Only the first fuse was cut from each of the serpentine springs, providing a vertical spring constant of 0.25 N/m. The plate mass was 0.47 μg and the vertical-mode resonant frequency was 3.7 kHz. The dc gain of the buffers was measured by injecting a signal at the buffer input. The measured gain of 0.983 is significantly smaller than the value predicted in Table II, due to a combination of a higher-than-expected pmos output conductance and a small parasitic load conductance across the buffer output.

We performed characterization of the testbed in air using Σ-Δ control of the vertical mode. One period of the modulated position sensor waveform, for various reference input values, is shown in Fig. 17. The interconnect leading off-chip has a capacitance value of about 10 pF, limiting the risetime to 424 ns. Tungsten contacts connecting the reference capacitor to the bridge were disconnected, due to HF attack during the microstructure release. The resulting imbalance in the capacitive divider produced a peak-to-peak sensor offset voltage of -103 mV and the source-follower driver circuit added a dc offset of -0.81 V. When the circuit was observed under an optical microscope, the dc level shifted negative to balance the reverse photocurrent in the diode at the buffer input. Both the signal amplitude and dc bias increase with displacement. The shift in dc bias arises from the nonlinear I–V characteristic of the forward-biased diode, since the modulated diode current must average to zero.

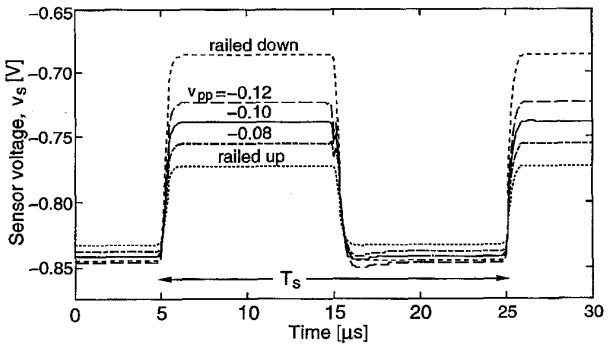

Fig. 17. One period of the modulated sensor voltage for various square-wave position reference input values. The peak-to-peak value of the reference input is indicated.

Plate displacement during closed-loop operation was measured by using laser interferometry between the plate and underlying substrate surfaces. Plate control of Δz motion, θ rotation, and ϕ rotation was observed. By estimating the blur envelopes of the interference patterns, tracking of vertical position and tilt was confirmed to be within ± 25 nm and $\pm 0.03°$, respectively. Stable position control was maintained up to the mechanical limit stops, which constrained motion to $-1.0\ \mu\mathrm{m} < \Delta z < +1.7\ \mu\mathrm{m}$.

Measured and calculated values of sensor output voltage versus displacement are compared in Fig. 18. Displacement measurement error was ± 25 nm; the corresponding sensor output error was ± 1 mV. Calculated sensor output values were computed from (7) using $C_{sv}|_{\Delta z=0} = 41.4$ fF, $C_{sf} = 4.0$ fF, $C_r = 6.8$ fF, and $C_p = 173$ fF. Interconnect overlap and fringe capacitance accounted for the reference and fixed sense capacitance. The effective parasitic capacitance value was about ten times less than the layout value, demonstrating the benefit of the driven shield. The laser illumination caused the input diode to be forward biased, thereby increasing the junction capacitance contribution to the parasitic capacitance and lowering the sensitivity. The measured sensitivity of the position sensor was 42 mV/μm at zero displacement. An ideal suspended parallel-plate electrostatic actuator in open-loop operation will become unstable when actuated beyond 1/3 of the undisplaced plate gap. In closed-loop operation of the testbed, the plate position was controlled far beyond the open-loop instability.

Measured feedthrough from the actuators to adjacent sensor nodes was a maximum of -61 dB, with two exceptions. In these two cases, the sensor high-impedance lines crossover the actuator interconnect. The extra parasitic capacitance increased

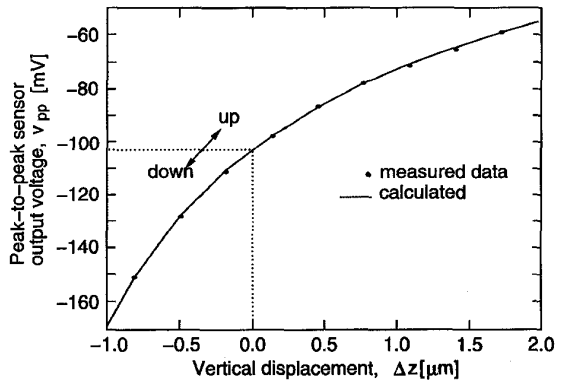

Fig. 18. Measured and calculated peak-to-peak sensor voltage versus plate displacement.

the feedthrough to 130 mV for 10 V of actuation voltage, which is significant when compared with the signal amplitude. In theory, the feedthrough voltage shift lasts through multiples of a sample period so the modulated position signal and closed-loop control should not be affected. In practice, the sampling rate was limited to about 50 kHz to allow the feedthrough to settle after an actuator is switched.

A measured value for vertical-mode damping of the plate was extracted from the open-loop step response at atmospheric pressure. The levitation force was generated by applying a 30-Hz square-wave voltage to the combs on both sides of the plate [18]. For small displacements around $\Delta z = 0$, the measured risetime was 2.8 ms corresponding to a damping factor, ζ_z, of 16. The holes reduce the squeeze-film damping to about 1/30th of the calculated value for a solid plate. Risetime measurements for varying comb-drive voltage indicate that the damping was reduced as the gap increases. Position dependence of the electrostatic forces from the comb-drive and from the sensor plates, however, was not determined with sufficient accuracy to deduce quantitative results of the second-order damping effects from the risetime measurements. Therefore, damping was approximated as a constant in the testbed simulations.

The simulated and measured closed-loop response to an 150-Hz square-wave position reference input is plotted in Fig. 19. Operation was at atmospheric pressure with a sampling rate of 50 kHz. The position-reference inputs (a) were stepped from 0 V to 56 mV, corresponding to a vertical plate displacement of 0.48 μm. Since all four position references were set to equal values, only the vertical (Δz) plate mode was excited. The simulated (b) and measured (c) peak-to-peak sensor voltage waveforms were in good agreement. The sensor signals tracked the position-reference voltages in steady-state operation. When the reference step was encountered, the plate rose to its new steady-state position in 0.6 ms, with a constant velocity of 0.8 mm/s due to the overdamped mechanical system. The fall time was slightly longer (0.8 ms) mainly due to asymmetric feedback voltages applied to the upper and lower actuators. Sensor noise voltage was detected when the position was locked to the reference and corresponded to a maximum plate vibration amplitude of approximately 25 nm, about 50 times larger than the total open-loop thermal noise of the plate in air. Based on the simulations and noise calculations, quantization noise is identified as the main contributor to the noise position. The simulated force acting on the plate is shown in Fig. 19(d). To first-order, the force was quantized into two states. Parallel-plate nonlinearity with position and force from the sensor electrodes, however, caused the total force to deviate from ideality. As the plate rose, the upper-actuator force level increased, while the lower-actuator force level was reduced. The ± 0.3 V modulation voltage impressed on the plate produced an actuator force component at the sampling frequency whose envelope is seen in the slewing portions of the force waveform. The modulation voltage across the sensor electrodes generated an additional dc pull-down force on the plate. A simulation of the averaged quantizer output (e) was formed by passing the simulated digital bitstream through a 10-kHz low-pass filter. The actual quantizer output (f) was measured by averaging 1024 sweeps of the comparator output on a digitizing oscilloscope. Different transient characteristics were produced on the simulated and measured waveforms as an artifact of the two different filtering methods. In both waveforms, the quantizer pulse density was nearly equal (around 50%) for both of the steady-state plate positions. Because of the force nonlinearity with position, however, the average electrostatic force was positive when the plate was pulled up and negative when the plate was pulled down.

Accelerometer performance was tested in air, with $f_s = 50$ kHz. In this operating mode, the position-reference voltages were fixed and the averaged output bitstreams provided a linear measure of external acceleration force. Only three of the four feedback loops were enabled to avoid an over-constrained system. The bitstreams were passed through a sinc^3 FIR filter, decimated by 500, and summed to provide an acceleration waveform for analysis. Measured acceleration noise was -86 dB/$\sqrt{\text{Hz}}$, referenced to a full-scale range of 55 g (0 dB). In a 50-Hz bandwidth, the measured noise floor was 19 mg, being dominated by quantization noise. Correlated noise of the individual bitstreams, corresponding to quantization noise in the rotational modes, was about 2.6 times larger than the acceleration noise floor. The measured correlated noise was somewhat higher than the estimated value and was unevenly spread among the bitstreams, due to the asymmetric system configuration.

VI. Conclusion

Digital control of a micromechanical plate was demonstrated for vertical and angular motion. Although the parallel-plate actuator force is highly nonlinear with position and voltage, the Σ-Δ feedback successfully controlled plate position to the mechanical limit stops. The simple and robust Σ-Δ architecture studied with the testbed has applications in multiaxis accelerometers, angular accelerometers, vibratory rate gyroscopes, and active mirror displays.

A general system simulation was formed by breaking the testbed into lumped-parameter electromechanical elements: a plate mass, springs, parallel-plate electrostatic actuators, and

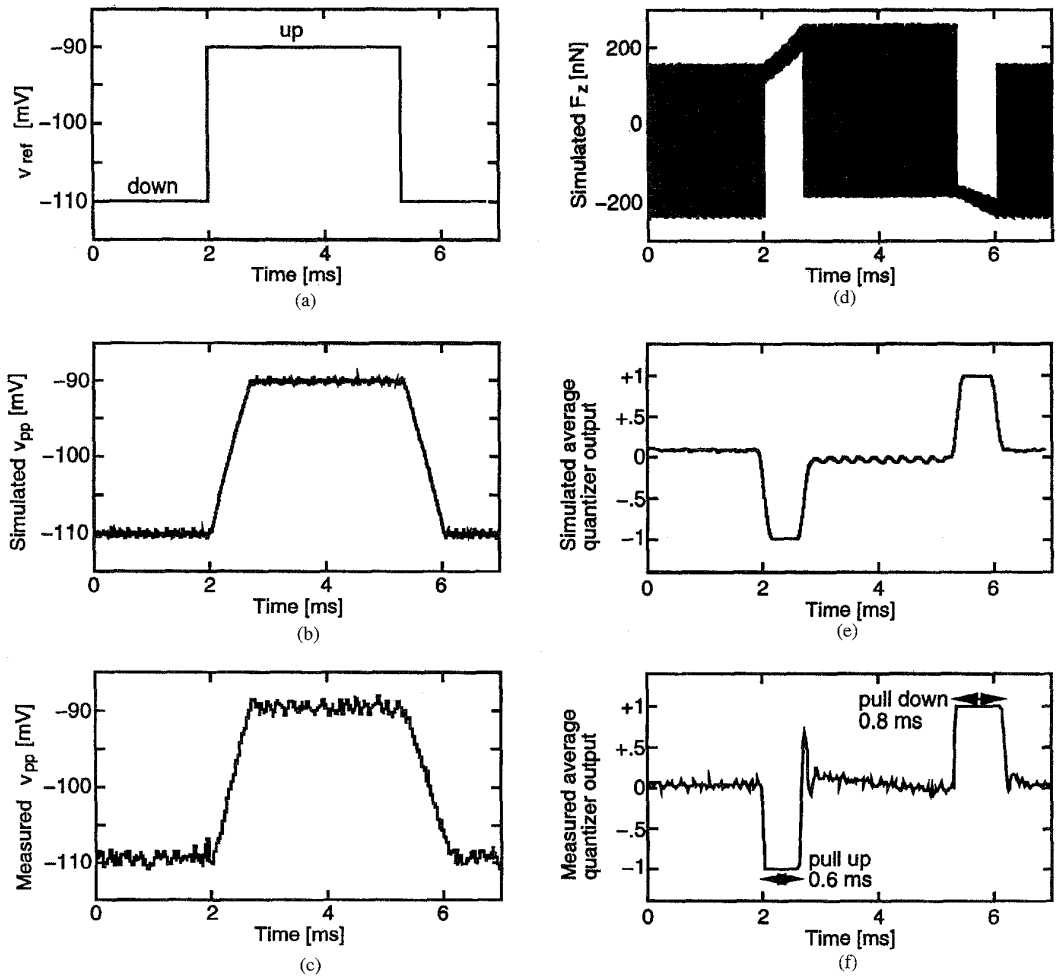

Fig. 19. Closed-loop response to an 150 Hz square-wave position reference input. (a) Position reference input voltage, v_{ref}. (b) Simulated peak-to-peak sensor voltage waveform, v_{pp}. (c) Measured v_{pp} waveform. (d) Simulated vertical force, f_z. (e) Simulated quantizer output, filtered through a 10-kHz low-pass filter. (f) Measured quantizer output, averaged over 1024 sweeps and normalized to ± 1.

capacitive sensors. Simple macro-models of these elements were sufficient to simulate the system dynamics effectively. The agreement of simulated and measured waveform demonstrates the viability of behavioral simulation for suspended MEMS. As MEMS become even more complex, this kind of system analysis will be necessary to explore design tradeoffs prior to layout.

For the testbed, accuracy of the position control was limited to ± 25 nm, due to quantization noise at the 50-kHz sampling rate. Integrated feedback circuitry is desirable to achieve a maximum possible sampling frequency and, therefore, to minimize quantization noise. Total noise acceleration is ultimately limited by the Brownian noise in air of 0.51 mg/$\sqrt{\text{Hz}}$. A higher sampling frequency is necessary to reduce the noise position to the total open-loop Brownian noise level in air of 0.56 nm. Future buffer designs should consider other means of dc biasing the input, since the diode junction capacitance dominates the effective parasitic capacitance to ground. The low-frequency equivalent diode noise voltage is significant and provides further motivation for eliminating the diode from the position-sensor circuit.

ACKNOWLEDGMENT

The authors would like to thank the U.C. Berkeley Microfabrication Facility. Special thanks to J. M. Bustillo, who helped with sensor processing and developed the SOG process sequence, S. Fang for completing the CMOS process steps, Dr. W. Yun for providing the initial micromechanical Σ-Δ design, W. A. Clark for helping construct the external electronics and proofreading the manuscript, and Prof. B. Boser for discussions on quantization noise.

REFERENCES

[1] W. Henrion, L. DiSanza, M. Ip, S. Terry, and H. Jerman, "Wide dynamic range direct digital accelerometer," in *Tech. Dig. IEEE Solid-State Sensor and Actuator Workshop*, Hilton Head, SC, June 1990, pp. 153–157.

[2] W. Yun, R. T. Howe, and P. R. Gray, "Surface micromachined, digitally force-balanced accelerometer with integrated CMOS detection

circuitry," in *Tech. Dig. IEEE Solid-State Sensor and Actuator Workshop*, Hilton Head, SC, June 1992, pp. 21–25.
[3] T. Smith, O. Nys, M. Chevroulet, Y. Decoulon, and M. Degrauwe, "A 15 b electromechanical sigma-delta converter for acceleration measurements," in *Tech. Dig. IEEE Int. Solid-State Circuits Conf.*, San Francisco, CA, Feb. 1994, pp. 160–161.
[4] C. Lu, M. Lemkin, and B. E. Boser, "A monolithic surface micromachined accelerometer with digital output," *IEEE J. Solid-State Circuits*, vol. 30, no. 12, pp. 1367–1373, Dec. 1995.
[5] B. E. Boser and R. T. Howe, "Surface micromachined accelerometers," *IEEE J. Solid-State Circuits*, vol. 31, no. 3, pp. 366–375, Mar. 1996.
[6] G. K. Fedder and R. T. Howe, "Integrated testbed for multi-mode digital control of suspended microstructures," in *Tech. Dig. Solid-State Sensor and Actuator Workshop*, Hilton Head, SC, June 1994, pp. 145–150.
[7] J. C. Candy and G. C. Temes, "Oversampling Methods for A/D and D/A Conversion" in *Oversampling Delta-Sigma Data Converters*. New York: IEEE Press, 1992, pp. 1–29.
[8] G. K. Fedder, J. C. Chang, and R. T. Howe, "Thermal assembly of polysilicon microstructures with narrow-gap electrostatic comb drive," in *Tech. Dig. IEEE Solid-State Sensor and Actuator Workshop*, Hilton Head, SC, June 1992, pp. 63–68.
[9] W. C. Tang, T.-C. H. Nguyen, and R. T. Howe, "Laterally driven polysilicon resonant microstructures," *Sens. Actuators*, pp. 25–32, Nov. 1989.
[10] M. W. Putty and K. Najafi, "A micromechanical vibrating ring gyroscope," in *Tech. Dig. Solid-State Sensor and Actuator Workshop*, Hilton Head, SC, June 1994, pp. 213–220.
[11] J. M. Bustillo, G. K. Fedder, C. T.-C. Nguyen, and R. T. Howe, "Process technology for the modular integration of CMOS and polysilicon microstructures," *Microsyst. Technol.*, pp. 30–41, Oct. 1994.
[12] G. K. Fedder, "Simulation of microelectromechanical systems," Ph.D. dissertation, Department of Electrical Engineering and Computer Sciences, Univ. of California, Berkeley, Sept. 1994, pp. 166–171.
[13] *ABAQUS User's Manual, 5.2 ed.*, Hibbitt, Karlsson & Sorenson, Inc., Pawtucket, RI, 1992.
[14] *HSPICE User's Manual, h9007 ed.*, Meta-Software, Inc., Campbell, CA, 1991.
[15] T. B. Gabrielson, "Mechanical-thermal noise in micromachined acoustic and vibration sensors," *IEEE Trans. Electron Devices*, vol. 40, pp. 903–909, May 1993.
[16] C. T.-C. Nguyen and R. T. Howe, "Quality factor control for micromechanical resonators," in *Tech. Dig. Int. Electron Devices Meet.*, San Francisco, CA, Dec. 1992, pp. 505–508.
[17] D. W. Burns, R. D. Horning, W. R. Herb, J. D. Zook, and H. Guckel, "Resonant microbeam accelerometers," in *Tech. Dig. 8th Int. Conf. Solid-State Sensors and Actuators (Transducers '95) and Eurosensors IX*, Stockholm, Sweden, June 1995, vol. 2, pp. 659–662.
[18] W. C. Tang, M. L. Lim, and R. T. Howe, "Electrostatic comb drive levitation and control method," *J. Microelectromech. Syst.*, pp. 170–178, Mar. 1992.

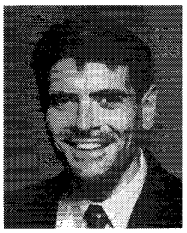

Gary K. Fedder (S'93–M'95) received the B.S. and M.S. degrees in electrical engineering from the Massachusetts Institute of Technology, Cambridge, in 1982 and 1984, respectively. In 1994, he received the Ph.D. degree in electrical engineering from the University of California, Berkeley, where his research focused on process development, modeling, and simulation for polysilicon surface microsystems.

He joined the faculty of Carnegie Mellon University, Pittsburgh, PA, in October 1994 as an Assistant Professor, holding a joint appointment with the Department of Electrical and Computer Engineering and the Robotics Institute. From 1984 to 1989, he was with the Hewlett-Packard Company on a VLSI integrated-circuit test system and on modeling of printed-circuit-board interconnect for high-speed computers. His present research interests include design and modeling of microsensors and microactuators, structured design methodologies for MEMS, microsensor packaging, and microrobotics.

Dr. Fedder received the 1993 AIME Electronic Materials Society Ross Tucker Award in recognition of his work on MEMS digital multimode control.

Roger T. Howe (S'79–M'84–SM'94–F'96) was born in Sacramento, CA, on April 2, 1957. He received the B.S. degree in physics from Harvey Mudd College, Claremont, CA, in 1979, and the M.S. and Ph.D. degrees in electrical engineering from the University of California, Berkeley, in 1981 and 1984, respectively.

He was on the faculty of Carnegie Mellon University, Pittsburgh, PA, during the 1984–1985 academic year, and was an Assistant Professor at the Massachusetts Institute of Technology, Cambridge, from 1985 to 1987. In 1987, he joined the Department of Electrical Engineering and Computer Sciences, University of California, Berkeley, where he is now a Professor, as well as Director of the Berkeley Sensor & Actuator Center. His research interests include silicon microsensors and microactuators, micromachining processes, and integrated-circuit design.

Dr. Howe served as Co-General Chairman of the 1990 IEEE Micro Electro Mechanical Systems Workshop and as General Chairman of the 1996 Solid-State Sensor and Actuator Workshop at Hilton Head, SC.